

frequency is in agreement with results for other species (6), and would be expected from the previous findings that the oscillation frequencies provide an indication of unit best frequencies and that unit best frequencies are closely related to an animal's discharge frequency (1, 2).

Starting 1 day after the initial DHT injection, all four experimental animals, both males and females, showed decreases in discharge frequency. The time course of the response in one of these animals, a female, is illustrated in Fig. 2a. To quantify the changes in discharge frequencies, we determined the difference between each individual's discharge frequency at the start and at the completion of the 2-week injection period ( $\Delta$ EOD). Females had higher discharge frequencies and showed larger  $\Delta$ EOD values than males. Also, females showed larger fractional changes (calculated by dividing  $\Delta$ EOD by the fish's initial discharge frequency). Control animals did not show such pronounced changes in discharge frequency (Fig. 2b).

The DHT treatment not only affected discharge frequency but also elicited changes in receptor oscillations. All four experimental fish exhibited declines in oscillation frequency which paralleled the declines in EOD frequency (Fig. 2a). Again, no such changes were apparent in the oscillations of the control animals. As a further test of DHT's influence, control animals from the first experiment were given DHT injections over a subsequent 2-week period. As in the first experiment, DHT caused decreases in discharge frequency and closely matched decreases in the frequency of oscillations.

Figure 2c summarizes the changes in EOD and oscillation frequencies for the experimental and control groups. The effect of DHT on discharge and oscillation frequencies was significantly different from that of saline ( $P < .01$ , Student's  $t$ -test). To determine the overall relation between the changes in EOD frequency and the changes in oscillation frequency we combined the results for the saline-treated and DHT-treated groups and performed a linear regression. The results of this analysis demonstrate a one-to-one correspondence between the changes.

The reduction in oscillation frequencies in *Sternopygus* by DHT indicates that the tuning characteristics of electroreceptors in these animals are dynamic and that electroreceptors are likely to show ontogenetic and seasonal changes corresponding to such changes in dis-

charge frequency. By means of this shift in receptor sensitivity, an individual can maintain maximum sensitivity to its changed motor output. This conclusion has since been confirmed by single-unit recordings from electroreceptive primary afferent fibers (10).

The mechanism underlying DHT's effect on receptor tuning remains to be determined. It is possible that electroreceptors are not directly affected by the steroid, but rather that their tuning characteristics are determined by the frequency of the electric field of the ongoing EOD. That is, steroids might affect only the EOD-generating circuitry; the changed electric field would then directly alter tuning. This hypothesis is compatible with the results of a study of pulse-discharging gymnotoids (12) in which it was noted that local variations in the peak powers of EOD's are matched by local changes in receptor tuning characteristics. Alternative proposals are (i) that steroids directly influence both the EOD-generating circuitry and receptor tuning and (ii) that steroids act directly on receptors, altering their tuning characteristics; the fish then modifies its discharge to match the best frequencies of its electroreceptors. Elucidation of the mechanism involved will shed light on the more general question of tuning in other vertebrate hair cells (13).

J. HARLAN MEYER

*Scripps Institution of Oceanography,  
A002, La Jolla, California 92093*

HAROLD H. ZAKON

*Neurobiology Unit, Scripps  
Institution of Oceanography, A001,  
and Department of Neurosciences,  
University of California, San Diego,  
La Jolla 92093*

## References and Notes

1. C. D. Hopkins, *J. Comp. Physiol.* **111**, 2 (1976); T. A. Viancour, *ibid.* **133**, 327 (1979).
2. H. Scheich, T. H. Bullock, R. H. Hamstra, *J. Neurophysiol.* **36**, 39 (1973); J. Bastian, *J. Comp. Physiol.* **112**, 165 (1976).
3. The discharge frequency of an individual *Sternopygus* is extremely constant, varying by less than 0.2 percent over days [T. H. Bullock, *Brain Behav. Evol.* **2**, 85 (1969)].
4. C. D. Hopkins, *Science* **176**, 1035 (1972); *Z. Tierpsychol.* **35**, 518 (1974).
5. J. H. Meyer, in preparation.
6. M. V. L. Bennett, in *Lateral Line Detectors*, P. H. Cahn, Ed. (Indiana Univ. Press, Bloomington, 1967), p. 313.
7. D. Watson and J. Bastian, *J. Comp. Physiol.* **134**, 191 (1979).
8. Aquariums were kept at  $26^{\circ} \pm 0.2^{\circ}\text{C}$  throughout the experiment by means of solid-state temperature controllers. Resistivity of the water was 1 kilohm-cm and pH was 6.5 to 7.0. The fish were maintained on a 12-hour light cycle.
9. Pulses (2 to 6 Hz) were passed through a stimulus isolation unit before entering the tank via the two carbon rods. Durations ranged from 0.2 to 20.0 msec, with the standard pulse being 1.0 msec. Amplitudes ranged from 1 to 20 mV/cm. The water in the tank was of the same resistivity, temperature, and pH as the water in the fish's home aquarium.
10. By utilizing a large-field stimulus and averaging, we recorded extracellular receptor potentials of many receptors from a patch of skin. This provides a consistent measure of receptor tuning, since the receptors are so similarly tuned in this species. Tuning, as determined by the oscillation frequency, is in very good agreement with the best frequencies of electroreceptive primary afferents (H. H. Zakon and J. H. Meyer, in preparation).
11. Saline solutions given to control animals consisted of two drops of Tween 80 per 50 ml of Ringer (6.48 g NaCl; 0.15 g KCl; 0.29 g  $\text{CaCl}_2 \cdot 2\text{H}_2\text{O}$ ; 0.12 g  $\text{MgSO}_4$ ; 0.084 g  $\text{NaHCO}_3$ ; 0.06 g  $\text{NaH}_2\text{PO}_4$  per liter of distilled water). DHT solutions were prepared by homogenizing DHT in the saline solution. Tween 80 was added to the saline to aid in the suspension of the steroid. Injections, consisting of 0.1 ml of saline or DHT solution (5  $\mu\text{g/g}$ ), were started 2 days after the baseline frequency determinations and were given for five consecutive days. A second series of five injections was given 2 days after the second determination of oscillation frequency.
12. J. Bastian, *J. Comp. Physiol.* **121**, 53 (1977).
13. R. Fettiplace and A. Crawford, *Proc. R. Soc. London Ser. B* **203**, 209 (1978).
14. We thank T. H. Bullock and W. Heiligenberg for critically reading the manuscript. Supported by NSF grants SPI80-16447 (H.H.Z.), BNS80-20829 (T.H.B.), and BNS76-20761 (W.H.) and by NIH grants NS00021-33 (T.H.B.) and PHSMH-2614904 (W.H.).

23 March 1982; revised 5 May 1982

## Computer-Assisted Mapping of Pyroclastic Surges

**Abstract.** *Volcanic hazard maps of surge boundaries and deposit thickness can be created by using a simplified eruption model based on an "energy line" concept of pyroclastic surge and flow emplacement. Computer image-processing techniques may be used to combine three-dimensional representations of the energy relations of pyroclasts moving under the influence of gravity (defined by an "energy cone") with digital topographic models of volcanoes to generate theoretical hazard maps. The deposit boundary and thickness calculated for the 18 May 1980 eruption of Mount St. Helens are qualitatively similar to those actually observed.*

Maps of volcanic hazards provide a basis for making policy decisions regarding public safety during times of impending volcanic crises. A useful map is one that is produced by methods that are (i) reliable (the data base should accurately reflect the distribution of products from all hazardous phenomena recorded by

outcrop patterns of prehistoric events, and observed phenomena of historic eruptions), (ii) applicable (an understanding of the phenomena should be sufficient to predict the distribution of products of renewed activity given adequate assumptions regarding the magnitude of the event, location of the vent,

and type of expected activity), (iii) flexible (the techniques of mapping should be adaptable to change as input from volcanic surveillance provides new information throughout a crisis period), and (iv) rapid (the methods should be simple so that maps can be produced with a minimum of effort in a realistic time frame relative to public safety needs).

For only a few volcanoes are hazard maps available that are adequate for use by public safety officials; these include the Cascade volcanoes (1-3), La Soufriere of Guadeloupe (4), and Vesuvius (5-7). The Mount St. Helens hazard maps (1) were excellent guides for formulating safety policy during the 1980 crisis. At La Soufriere, on the other hand, the map

(4) was not completed until well after major policy decisions related to safety had been made. There are many active volcanoes in populated regions where hazard maps would be of immediate benefit. Current methods of compilation require several years to develop a single map. We propose here a technique of map generation that has the advantages of being reliable, applicable, flexible, and rapid. In this technique computer image-processing methods are used to combine a three-dimensional model of a simplified expression of the energy relations in volcanic deposit emplacement with a digital model of the surface topography. The result is a map of the distribution of the effects and deposits of an eruption.

We have modeled the effects of pyroclastic surge eruptions, that is, eruptions that produce suspensions of pyroclastic particles in a turbulent gaseous matrix which behave like gravity-driven flows of cohesionless grains (8). In this type of eruption the particulate material rapidly decelerates as it is explosively shot upward from the vent; zero vertical velocity is reached within 500 to 1500 m. Gravity then causes the dense suspension to fall downward. During fallback, potential energy is converted into kinetic energy. On the ground surface the mass moves in the direction of greatest flow potential as the gravitational force is balanced by the inertial force of the flow plus frictional resistance. Thus a type of Bernoulli equation of motion (9) can be applied to the system.

Heim (10) first applied this method of analysis to mass flowage of landslides [see also (11)]. He considered the line connecting the top of the landslide mass before movement to the toe of the deposit as an "energy line." A coefficient  $\mu$  (equal to the tangent of the slope of this line relative to the horizontal), in conjunction with the topographic surface, constrains the dynamic properties of the model. Heim pointed out that the slope of the energy line is dependent on the volume of the fallen mass: the larger the landslide, the smaller the slope of the line. Sheridan (12) used this approach to estimate the energy line slope for pyroclastic flows and steam-blast deposits. Values for the largest ash-flow tuffs range between 11° and 4°, with 7° being typical. An energy line analysis (13) can be extended to calculate acceleration, velocity, and runout time for pyroclastic flows and surges by assuming appropriate boundary conditions.

In our application we need a three-dimensional representation of the energy line. As a first approximation we use a

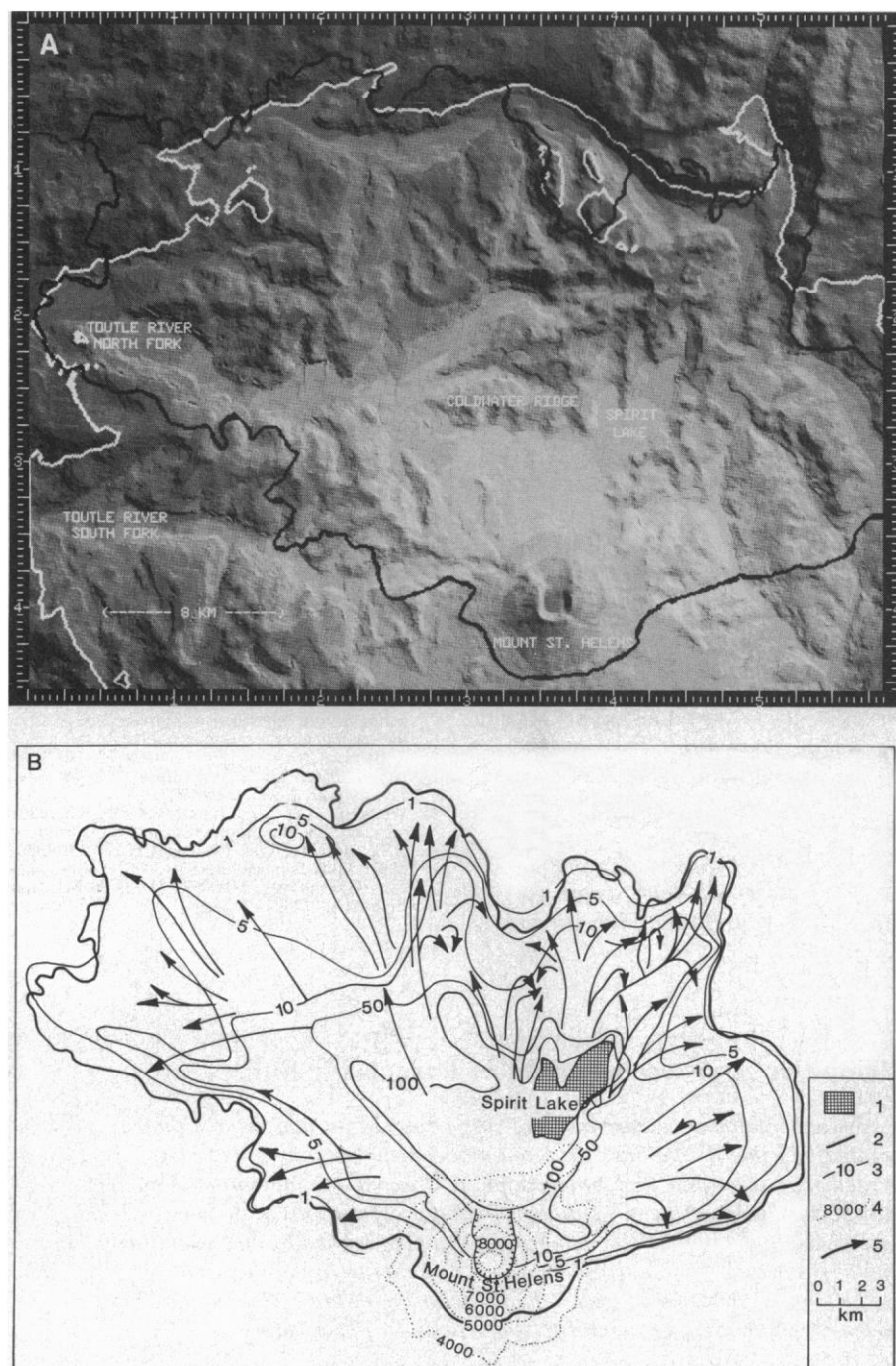


Fig. 1. Comparison of computer-generated images of Mount St. Helens 1980 deposits with characteristics known from field studies. White boundary in the computer-generated map (A) is the intersection with the topography of a 7° energy cone with its apex ~ 1.5 km north of the summit at an altitude of 11,500 feet (3505 m) above sea level. Gray levels within boundary are equal increments in the numerical difference between the altitude of the cone and the altitude of the topography. Black outline is the observed margin of the blast zone. Key for the Mount St. Helens map (B): 1, Spirit Lake; 2, outer margin of the blast zone from (16); 3, isopach contours of total deposit thickness in centimeters (16); 4, elevation of the volcanic edifice in feet; and 5, flow directions of the blast determined by tree blowdown (16).

cone with a central depression angle equal to the assumed slope of the energy line (13). The cone's apex height is set equal to the height to which material is thrust above the vent. The flowage potential is strongly controlled by the elevation difference between the "energy cone" and the ground surface: flow should cease where the two are equal. Because such gravity flows are strongly influenced by topographic gradient, the surge cloud would not reach its maximum extent in all directions. Rather, the mass flux would be greatest in areas of steepest negative gradient.

Digital topography is the principal empirical data set. For this study, the National Cartographic Information Center (NCIC) 1° by 2° digital terrain model of the Hoquiam (NL10-5) quadrangle was used. This model consisted of 1220 east-west lines by 1755 16-bit samples north-south, with a spatial resolution of about 215 feet per picture element, a vertical precision of 1 foot, a vertical accuracy of  $\pm 33$  feet, and included heights between 20 and 9680 feet. These data were in continuous tone rather than in contour or grid format.

A continuous tone, gray level representation of the surface of the energy cone was generated by a program that allowed the apex location, apex height, slope, and ground resolution to be specified. The calculation was performed in 16-bit format, and the ground resolution and altitude increments were selected to match those of the topographic data set (for example, 215 feet ground resolution, and altitude in feet, for the NCIC 1° by 2° quadrangle). Both the topography and cone were reduced from 16-bit to 8-bit format for ease in processing and display. They were reduced by the same factor to ensure correct slope relations. To find the intersection of the energy cone with the topography, the latter was subtracted from the former: values greater than zero occur where the cone exceeds the topography. Additional programs were used to highlight the boundary and to present the difference image in contour format.

A shaded relief image of the topography was also made (14). This image resembles a physical relief model of the topography and provides an excellent base map.

Figure 1 shows the results of a model eruption of Mount St. Helens in which the energy cone apex is located approximately 1.5 km north of the summit and at an altitude of 11,500 feet above sea level (3500 feet or 1066 m above ground level). The angle of the cone is 7°. This location and height are consistent with observa-

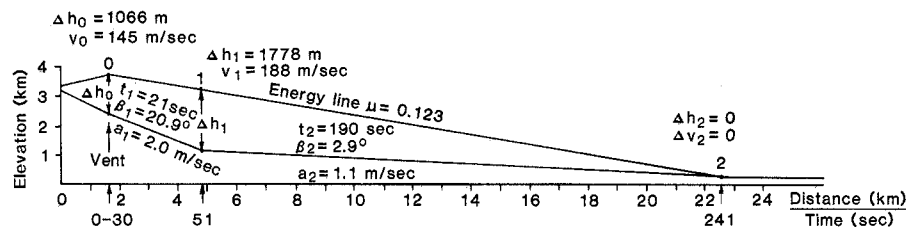


Fig. 2. Generalized energy line data for the 18 May 1980 surge of Mount St. Helens computed as discussed in (13). Here  $t_1$ ,  $\beta_1$ , and  $a_1$  are runout time, slope, and acceleration on the volcanic cone;  $t_2$ ,  $\beta_2$ , and  $a_2$  are comparable data on the apron surrounding the volcano; and  $v_0$ ,  $v_1$ , and  $v_2$  are the potential velocities at the vent, base of the edifice, and margin of the deposit, assuming that for a ground-hugging surge all the potential energy is converted to a near-horizontal velocity component. The elapsed time of 30 seconds at the vent is due to vertical uplift and fallback of the dense cloud.

tions of the Mount St. Helens eruption [for example, (15)]. The height and slope are also consistent with values found by Sheridan (12) from field studies at other volcanoes. The sinuous outer margin shows the variation in the position of the intersection of the energy cone and the surface topography. Its outline is generally similar to the observed margin of the effects of the Mount St. Helens eruption (16), although symmetrical about the cone apex and not limited only to the area north of the mountain as are the actual effects. The contours represent equal increments of the difference between the elevation of the cone and the topography. They appear to mimic the observed contours of deposit thickness (16).

Figure 2 shows a time line of events based on the simplified model (12). Important features are (i) the vertical rise time to the apex of the cone ( $\sim 15$  seconds) and the comparable time needed to fall (elapsed time,  $\sim 30$  seconds), (ii) the velocity at the point where material begins to move downslope ( $\sim 145$  m/sec), (iii) the velocity at the base of the mountain ( $\sim 188$  m/sec) and the elapsed time needed to reach that location ( $\sim 51$  seconds), and (iv) the elapsed time to the final distance (zero velocity;  $\sim 241$  seconds). These values compare favorably with those determined by observation (15-17) even though the numerical technique does not address any specific details of the eruption phenomena.

This example is not a unique solution to our model of the eruption phenomena at Mount St. Helens. Because of the short calculation time required for each model, we were able to investigate many combinations of the energy cone parameters. In general, solutions with apex heights between 500 and 1500 m and slopes between 5° and 9° gave margins comparable to that actually observed, with individual minor variations depending on the exact nature of the local topography.

Our simple model of pyroclastic surge appears consistent with the events and deposits of the 18 May 1980 eruption of Mount St. Helens (15-17). The match of calculated and actual distal boundaries, the inferred deposit thickness, and the intrinsic symmetry of the model suggest that the initial pyroclastic event in this eruption was not necessarily laterally directed. Rather, the northward-oriented phenomena could have been the natural result of the movement of a gravity-driven density flow resulting from the topography of the north slope of the volcano as modified by the rockslide avalanche that preceded the eruption (18). In this scheme, directed jetting within the initial ejection of pyroclasts gave rise only to small variations in the radial distance of the surge effects.

MICHAEL C. MALIN

MICHAEL F. SHERIDAN

Department of Geology,  
Arizona State University,  
Tempe 85287

#### References and Notes

1. D. R. Crandell and D. R. Mullineaux, *U.S. Geol. Surv. Bull.* 1383-C (1978).
2. \_\_\_\_\_, C. D. Miller, in *Volcanic Activity and Human Ecology*, P. D. Sheets and D. K. Grayson, Eds. (Academic Press, New York, 1979), pp. 195-219.
3. C. D. Miller, *U.S. Geol. Surv. Bull.* 1503 (1980).
4. D. Westercamp, *Bull. Volcanol.* 43, 431 (1980).
5. G. P. L. Walker, in *I Volcani attivi dell'area Napoletana* (Provincial Administration, Naples, 1977).
6. M. Rosi, R. Santacroce, M. F. Sheridan, *Bull. Rech. Geol. Miner.*, in press.
7. F. Barberi, M. Rosi, R. Santacroce, M. F. Sheridan, in *Volcanic Hazards*, H. Tazieff, Ed. (Elsevier, Amsterdam, in press).
8. A large number of other types of phenomena can be modeled as gravity-driven flows. They include landslides of many forms, lava flows, debris and mud flows, and snow avalanches. Thus, this technique is applicable to several other processes recognized as posing volcanic hazards, as well as to nonvolcanic geologic hazards analyses.
9. L. Prandtl and O. G. Tietjens, *Fundamentals of Hydrodynamics and Aeromechanics* (Dover, New York, 1957).
10. A. Heim, *Z. Dtsch. Geol. Ges.* 34, 74 (1882); *Bergsturz und Menschenleben* (Fritz und Wasmuth, Zurich, 1932).
11. K. J. Hsü, *Geol. Soc. Am. Bull.* 86, 129 (1975); in *Rockslides and Avalanches*, vol. 1, *Natural Phenomena*, B. Voight, Ed. (Elsevier, New York, 1978), pp. 71-93.
12. M. F. Sheridan, *Geol. Soc. Am. Spec. Pap.* 180, 125 (1979); *Bull. Volcanol.* 43, 397 (1980).

13. Our analysis of flow results from superimposing an energy cone onto a computer image of the ground surface. The elevation and slope of the cone relative to the elevation and slope of the topography give the acceleration (deceleration), velocity, and runoff time of the surge. The main parameters for motion parallel to ground surface are calculated from three equations:

$$a(i) = g(\sin \beta - \mu \cos \beta)$$

where  $a(i)$  is the surge acceleration,  $g$  is the acceleration due to gravity,  $\beta$  is the slope of the land surface, and  $\mu$  is the Heim coefficient (tangent of the energy line slope),

$$v^2(i) = v_0^2 + 2 a(i) s(i)$$

where  $v(i)$  is the velocity,  $v_0$  is the initial velocity, and  $s(i)$  is the slope distance, and

$$t(i) = 2 s(i)/[v_0 + v(i)]$$

where  $t(i)$  is the runoff time. The results of this simple approach, schematically applied to the Mount St. Helens blast, are shown in Fig. 2. These values compare well with those observed [for example, see (17)]. The difference between the elevation of the energy surface and the

ground topography,  $\Delta h(i)$ , directly yields the potential component velocity provided the surge is truly ground-hugging:

$$v(i) = [2g\Delta h(i)]^{1/2}$$

Taking boundary conditions into consideration, the total flow field vectors and streamlines and mass deposition per unit area can also be computed.

14. R. M. Batson, K. Edwards, E. M. Eliason, *J. U.S. Geol. Surv.* **3** (No. 4), 401 (1975).  
 15. B. Voight, *U.S. Geol. Surv. Prof. Pap.* **1250** (1981), pp. 69–86.  
 16. S. W. Kieffer, *Nature (London)* **291**, 568 (1981); *U.S. Geol. Surv. Prof. Pap.* **1250** (1981), pp. 379–400; R. P. Hoblitt, C. D. Miller, J. W. Vallance, *ibid.*, pp. 401–419; J. G. Moore and T. W. Sisson, *ibid.*, pp. 421–438; R. B. Waitt, Jr., *ibid.*, pp. 438–450.  
 17. C. J. Rice and D. K. Watson, *Eos* **62**, 557 (1981).  
 18. B. Voight, H. Glicken, R. J. Janda, P. M. Douglass, *U.S. Geol. Surv. Prof. Pap.* **1250** (1981), pp. 347–377.

30 November 1981; revised 12 May 1982

## Venus: Global Surface Radar Reflectivity

**Abstract.** *Observations of the surface of Venus, carried out by the Pioneer Venus radar mapper at a wavelength of 17 centimeters, reveal a global mean reflectivity at normal incidence of  $0.13 \pm 0.03$ . Over the surface, variations from a low of  $0.03 \pm 0.01$  to a high of  $0.4 \pm 0.1$  are found, with Theia Mons, previously identified as possibly volcanic, showing a value of  $0.28 \pm 0.07$ . Regions of high reflectivity may consist of rocks with substantial inclusions of highly conductive sulfides.*

The radar altimeter ( $I$ ) carried aboard the Pioneer Venus Orbiter spacecraft is capable of determining three characteristics of that planet's surface: relief, roughness, and reflectivity. Results for the first two of these have been presented (2, 3); here we discuss some initial findings on reflectivity.

For small angles,  $\theta$ , of departure from normal incidence to the mean resolved surface, a scattering law first derived by Hagfors (4) appears to provide a useful approximation to the observed echo strength. Over the range  $0 \leq \theta \leq 10^\circ$ , to which altimeter observations are limited (1), this law may be written

$$\sigma_0(\theta) \approx (\alpha^{-2} \rho/2) (\cos^4 \theta + \alpha^{-2} \sin^2 \theta)^{-3/2} \quad (1)$$

where  $\sigma_0$  is the dimensionless specific radar cross section (actual radar cross section divided by associated surface area),  $\rho$  is the power reflectivity at normal incidence to a smooth surface, and  $\alpha$  is the root-mean-square (r.m.s.) inclination (in radians) of coherently reflecting surface facets having dimensions larger than the observing wavelength (17 cm). We used the observed distribution of echo power in delay, converted to a distribution in the angle of incidence through the known observing geometry, to estimate the parameters  $\rho$  and  $\alpha$  associated with each altimetric observation. Because of the restriction on  $\theta$ , values of  $\alpha$  larger than  $0.17$  ( $10^\circ$ ) are poorly determined.

Figure 1 represents the near-global smoothed distribution of reflectivity for the surface of Venus obtained from the radar altimeter over the period of its operation from 5 December 1978 through 18 March 1981. Comparable distributions of relief and of the slope parameter  $\alpha$  (but for a smaller data set) are given in (3) as plate 1 and figure 4, respectively. The lateral resolution of the surface ("footprint") inherent in these measurements varies with spacecraft altitude as detailed in table 2 of (3), but has been smoothed to about 100 km in all the global maps.

The mean global reflectivity obtained from these observations (weighted by area) is  $0.13 \pm 0.03$  (5), a result consistent with the far more restricted Earth-based radar observations (6). Excursions in reflectivity from a low of about  $0.03 \pm 0.01$  to a high of  $0.4 \pm 0.1$  are observed for the data shown in Fig. 1. These values have not yet been corrected for the possible presence of diffusely scattering material, which can reduce the surface area effective in the quasi-specular reflecting process below that calculated geometrically. To the extent such correction is required, the estimated reflectivity is increased. The amount of diffusely scattering surface material may be determined, at least approximately, from radar data taken at relatively high angles of incidence as well as from measurements of the depolarized echo component (7).

For a single surface layer, whose magnetic permeability is unity, the reflectivity is controlled solely by the complex dielectric discontinuity presented at the reflecting interface, and may be expressed as

$$\rho = |(1 - \epsilon^{1/2})/(1 + \epsilon^{1/2})|^2 \quad (2)$$

where  $\epsilon = K + i[L + S/(\epsilon_0 \omega)]$  is the complex dielectric constant of the bulk surface material. The real component,  $K$ , dominates the reflectivity for most dry terrestrial rocks and soils. The imaginary component depends in part on the dielectric loss,  $L$ , and in part on the volume conductivity,  $S$ , as well as on the permittivity of free space,  $\epsilon_0$ , and the angular frequency of the incident radiation,  $\omega$ . At radar frequencies ( $\sim 10^9$  Hz),  $S$  must exceed about 0.1 mho/m to affect the reflectivity significantly; most dry terrestrial surface materials (except sulfide minerals) have  $S$  between  $10^{-2}$  and  $10^{-6}$  mho/m (8) and  $L$  of the order of 0.05 to 0.2 (9).

The bulk dielectric constant is controlled in part by the porosity and in part by the electrical properties of the constituents of the surface material. In general, for very porous or powdered material,  $K$  is low (typically 2.0 for a density of 1 g/cm<sup>3</sup>) and largely independent of the type of material (9). For solid, dry terrestrial rocks at radar frequencies, on the other hand,  $K$  varies from about 5 for most granites up to as much as 9 for some basalts (8); for meteoritic material containing metallic and sulfide inclusions, the dielectric constant rises substantially above 9 (9).

To look for the extent to which the scatter in the observations might exceed the statistical fluctuations inherent in the data, we plotted each value of  $\rho$  in a given surface region against its conjugate value of  $\alpha$ , both having been estimated simultaneously from a fit of Eq. 1 to the data of a given observation. The ensemble of points corresponding to the selected group of observations forms a scatter diagram and provides a useful way not only of confirming correlations between the estimated parameters but also of illustrating the internal consistency of the data set. The location of the centroid of the ensemble on the diagram categorizes the surface in terms of its gross radar scattering properties.

Figure 2 shows scatter diagrams drawn from the observational data for two selected areas of the surface. The first covers a major portion of Sedna Planitia and is fairly typical not only of the Venus lowlands but of most of the rolling uplands as well. The mean value of  $\rho$  for this region is  $0.12 \pm 0.03$ , corre-